

Accelerated Article Preview

Low-loss contacts on textured substrates for inverted perovskite solar cells

Received: 28 June 2023

Accepted: 12 October 2023

Accelerated Article Preview



Cite this article as: Park, S. M. et al.

Low-loss contacts on textured substrates for inverted perovskite solar cells. *Nature* <https://doi.org/10.1038/s41586-023-06745-7> (2023)

So Min Park, Mingyang Wei, Nikolaos Lempesis, Wenjin Yu, Tareq Hossain, Lorenzo Agosta, Virginia Carnevali, Harindi R. Atapattu, Peter Serles, Felix T. Eickemeyer, Heejong Shin, Maral Vafaie, Deokjae Choi, Kasra Darabi, Eui Dae Jung, Yi Yang, Da Bin Kim, Shaik M. Zakeeruddin, Bin Chen, Aram Amassian, Tobin Filleter, Mercuri G. Kanatzidis, Kenneth R. Graham, Lixin Xiao, Ursula Rothlisberger, Michael Grätzel & Edward H. Sargent

This is a PDF file of a peer-reviewed paper that has been accepted for publication. Although unedited, the content has been subjected to preliminary formatting. Nature is providing this early version of the typeset paper as a service to our authors and readers. The text and figures will undergo copyediting and a proof review before the paper is published in its final form. Please note that during the production process errors may be discovered which could affect the content, and all legal disclaimers apply.

1 **Low-loss contacts on textured substrates for inverted perovskite solar cells**

2 So Min Park^{1,2,10}, Mingyang Wei^{3,10}, Nikolaos Lempesis^{4,10}, Wenjin Yu⁵, Tareq Hossain⁶, Lorenzo
3 Agosta⁴, Virginia Carnevali⁴, Harindi R. Atapattu⁶, Peter Serles⁷, Felix T. Eickemeyer³, Heejong
4 Shin¹, Maral Vafaie², Deokjae Choi¹, Kasra Darabi⁸, Eui Dae Jung², Yi Yang¹, Da Bin Kim², Shaik
5 M. Zakeeruddin³, Bin Chen¹, Aram Amassian⁸, Tobin Filleter⁷, Mercouri G. Kanatzidis¹, Kenneth
6 R. Graham⁶, Lixin Xiao⁵, Ursula Rothlisberger⁴, Michael Grätzel^{3†} & Edward H. Sargent^{1,2,9†}

7 ¹Department of Chemistry, Northwestern University, Evanston, Illinois 60208, United States.

8 ²Department of Electrical and Computer Engineering, University of Toronto, Toronto, Ontario,
9 M5S 3G4, Canada.

10 ³Laboratory of Photonics and Interfaces, Ecole Polytechnique Fédérale de Lausanne, Lausanne,
11 1015, Switzerland.

12 ⁴Laboratory of Computational Chemistry and Biochemistry, Ecole Polytechnique Fédérale de
13 Lausanne, Lausanne, 1015, Switzerland.

14 ⁵State Key Laboratory for Artificial Microstructure and Mesoscopic Physics, Department of
15 Physics, Peking University, Beijing 100871, P. R. China.

16 ⁶Department of Chemistry, University of Kentucky, Lexington, KY, 40506, United States.

17 ⁷Department of Mechanical and Industrial Engineering, University of Toronto, Toronto, Ontario,
18 M5S 3G8, Canada.

19 ⁸Department of Materials Science and Engineering, and Organic and Carbon Electronics
20 Laboratories (ORaCEL), North Carolina State University, Raleigh, NC, 27695, United States.

21 ⁹Department of Electrical and Computer Engineering, Northwestern University, Evanston, Illinois
22 60208, United States.

23 ¹⁰These authors contributed equally to this work: So Min Park, Mingyang Wei, Nikolaos Lempesis

24 †e-mail: ted.sargent@northwestern.edu; michael.gratzel@epfl.ch

25

26 Inverted perovskite solar cells (PSCs) promise enhanced operating stability compared to
27 their normal-structure counterparts¹⁻³. To improve efficiency further, it is crucial to
28 combine effective light management with low interfacial losses^{4,5}. Here we develop a
29 conformal self-assembled monolayer (SAM) as the hole-selective contact on light-managing
30 textured substrates. Molecular dynamics simulations indicate cluster formation during
31 phosphonic acid adsorption leads to incomplete SAM coverage. We devise a co-adsorbent
32 strategy that disassembles high-order clusters, thus homogenizing the distribution of
33 phosphonic acid molecules, thereby minimizing interfacial recombination and improving
34 electronic structures. We report a lab-measured power-conversion efficiency (PCE) of 25.3%
35 and a certified quasi-steady-state PCE of 24.8% for inverted PSCs, with a photocurrent
36 approaching 95% of the Shockley-Queisser maximum. An encapsulated device having a PCE
37 of 24.6% at room temperature retains 95% of its peak performance when stressed at 65°C
38 and 50% relative humidity following >1000 hours of maximum power point tracking under
39 1-sun illumination. This represents one of the most stable PSCs subjected to accelerated
40 ageing – achieved with a PCE surpassing 24%. The engineering of phosphonic acid
41 adsorption on textured substrates offers a promising avenue for efficient and stable PSCs. It
42 is also anticipated to benefit other optoelectronic devices that require light management.

43 Perovskite solar cells (PSCs) have recently attained a certified efficiency of 26.1%⁶; however, the
44 very highest PCE devices have yet to meet operating stability under accelerated ageing tests⁵. The
45 limited device stability is attributed to the presence of mobile and hygroscopic p-type dopants in
46 hole-transporting layers, which undermine moisture and thermal stability⁷. Inverted PSCs present
47 a solution by utilizing undoped hole-selective contacts⁸. Recent studies have shown PCEs
48 surpassing 25% for inverted PSCs². However, when adhering to the stringent quasi-steady-state
49 (QSS) protocol, their certified efficiency (~24%) requires further improvement^{3,9}.

50 Efforts to improve inverted PSC efficiency have focused on interface passivation^{2,9,10}. This
51 approach suppresses non-radiative recombination and thus improves fill factors and
52 photovoltages¹¹. Nevertheless, higher photocurrents are needed for efficiency gains. In normal-
53 structure PSCs, this has been realized using textured fluorine-doped tin oxides (FTO) as the
54 transparent conductive oxides (TCO)^{4,5}. The pyramidal grains on FTO minimize reflection losses
55 and extend the length of the average optical path⁴. By contrast, inverted PSCs, often built on
56 smooth indium tin oxides (ITO)^{9,10}, face substantial optical losses due to the lack of light
57 management.

58 The discrepancy is ascribed to differences in transporting materials and deposition techniques. In
59 normal-structure PSCs, inorganic hole-blocking layers are conformally deposited on textured
60 substrates using spray pyrolysis and chemical bath deposition^{4,5}. However, inverted PSCs typically
61 employ ultra-thin (<5 nm) organic hole-selective contacts on substrates^{2,3}, which can be
62 challenging to deposit uniformly using solution processing¹². Inhomogeneity leads to energy losses
63 and insufficient carrier extraction¹³.

64 Self-assembled monolayers (SAMs), particularly those composed of phosphonic acid molecules
65 with hole-selective tail groups, have shown promise in addressing this issue¹⁴. Phosphonic acids
66 establish coordinative/covalent bonds with TCOs, allowing for sufficient SAM coverage on rough
67 surfaces¹⁵. This could provide a low-loss interface, uniting light management with interface
68 passivation. Indeed, photocurrent improvements have been observed when replacing SAM-
69 modified ITO with FTO substrates in inverted PSCs¹⁶.

70 Despite the promise, achieving a high-density, closely packed SAM remains challenging, which
71 leads to erratic interfacial properties¹⁷. For example, M. Liu et al. revealed that phosphonic acids
72 failed to fully cover textured wafers, which affected the performance of tandem solar cells¹⁸. Even

73 on flat substrates, the formation of SAMs tends to be non-uniform, a problem usually attributed to
74 the limited solubility of phosphonic acids¹⁹ and their insufficient chemical bond formation with
75 metal oxides²⁰.

76 Several strategies have been proposed to ensure conformal SAM coverage, such as utilizing more
77 reactive oxide surfaces (e.g., nickel oxides) to promote hetero condensation¹⁸, employing thermal
78 evaporation for SAM deposition²¹, and designing highly soluble phosphonic acid molecules¹⁹.
79 However, these methods can be laborious, requiring time-intensive molecule design, synthesis,
80 and vacuum-based layer deposition. Additionally, the use of highly reactive oxides could
81 compromise device stability due to redox reactions with ammonium halides²².

82 **Molecular dynamics simulations**

83 We sought to deepen understanding of how phosphonic acids interact with textured TCOs. We
84 began by looking at the case of 2-(9H-carbazol-9-yl)ethyl)phosphonic acid (2PACz), an organic
85 molecule (Fig. 1a) capable of forming SAMs on TCOs¹⁴, and investigated its interactions with
86 FTO. 2PACz has found extensive applications as a hole-selective contact in PSCs in view of its
87 excellent defect passivation and deep highest occupied molecular orbital (HOMO) level²¹. The
88 surface properties of FTO were approximated using tin oxides (SnO₂), given that commercial FTO
89 has a fluorine-doping level under 0.5% (atomic percentage)²³. Flat vs. corrugated SnO₂ were
90 analysed to understand the effects of surface morphology (Supplementary Fig. 1).

91 Molecular dynamics (MD) simulations suggest that 2PACz molecules can agglomerate, forming
92 dimers, trimers, and tetramers (Fig. 1b and Supplementary Fig. 2). Within the initial 1 nanoseconds
93 of simulations, 90% of the final number of clusters has been reached (Fig. 1b), and dimers were
94 the most prevalent among clusters (Fig. 1c). Compared to flat surfaces, textured surfaces led to
95 more clusters (e.g., 7 vs. 0 for 20 2PACz molecules on 6-nm-wide SnO₂) (Supplementary Note 1;
96 Supplementary Figs. 3 and 4). The cluster formation is closely linked to the inhomogeneity of
97 SAMs on FTO. For instance, when 162 2PACz molecules are positioned on top of textured SnO₂
98 surfaces, despite their initial random distribution (Supplementary Video 1), the final equilibrated
99 structures exhibit clear phase segregation (Fig. 1d), where almost 85% of the SnO₂ surface remains
100 uncovered by any 2PACz molecules (Supplementary Fig. 5). These observations were also verified
101 in a larger system (22-nm width; 1134 2PACz molecules) (Supplementary Fig. 6).

102 Reasoning that a thiol group (–SH) could interact with phosphonic acids, and a carboxyl group
103 (–COOH) attached to FTO, we introduced 3-mercaptopropionic acid (3-MPA) (Fig. 1a) in
104 simulations to break apart 2PACz clusters particularly on textured substrates. The approach is akin
105 to the co-adsorbent strategy used in dye-sensitized solar cells to reduce dye aggregation on
106 titanium oxides²⁴. Similar strategies have been employed to improve the quality of hole-selective
107 SAMs^{25,26}. With 3-MPA at a molar ratio of 1:9 with 2PACz, we saw a relative 15% decrease in
108 the number of clusters on textured surfaces (Fig. 1b), and a slower formation rate (20 ns⁻¹ vs. 28
109 ns⁻¹) (Supplementary Fig. 7). In particular, the higher-order clusters (trimers and tetramers)
110 decreased by 53% (Fig. 1c). As a result, the mixed system shows less phase segregation (Fig. 1e
111 and Supplementary Video 2), leading to extended surface coverage (67% vs. 15%) by 2PACz
112 molecules (Supplementary Fig. 5). Ab initio MD (AIMD) simulations (Supplementary Note 2 and
113 Supplementary Fig. 8) indicate that the presence of 3-MPA hinders the free movement of
114 individual 2PACz molecules by forming a supramolecular structure (Fig. 1f). This reduces
115 agglomeration with already-formed dimers, suppressing the formation of higher-order clusters
116 (Supplementary Video 3). Density functional theory (DFT) calculations revealed surface binding
117 energies of –3.2 eV and –2.6 eV for 2PACz and 3-MPA, respectively, which are much stronger
118 than the interaction energies of 2PACz clusters (–0.3 to –0.1 eV per molecule). This indicates
119 robust anchoring of 2PACz and 3-MPA molecules upon contact with substrate surfaces.

120 **Characterization of organic contacts**

121 We deposited both 2PACz and a mixture of 2PACz:3-MPA on FTO substrates using solution
122 processing, followed by annealing the film at 100°C and solvent washing (Methods). Micelles
123 were detected in the processing solutions through dynamic light scattering (DLS) (Supplementary
124 Fig. 9). However, due to their limited proportion in the volume distribution compared to 2PACz
125 monomers, film formation primarily resulted from molecular diffusion rather than direct micellar
126 adsorption²⁷.

127 The film composition and its interaction with FTO substrates were investigated using X-ray
128 photoelectron spectroscopy (XPS) and attenuated total reflectance Fourier transform infrared
129 spectroscopy (ATR-FTIR), respectively. For the film comprising solely 2PACz molecules (the
130 control), the presence of 2PACz was evidenced by the appearance of the phosphine (P) doublet
131 peak (Fig. 2a) and the characteristic C-N peak and C-C/C-H peak (Supplementary Fig. 10) in the

132 XPS spectra²¹. In the case of mixed film, 3-MPA was indicated by the sulfur (S) 2*p* doublet peak
133 at around 163.8 eV (i.e., the thiol group) (Fig. 2a)²⁸. From ATR-FTIR, bidentate or tridentate
134 binding was identified as the mode of 2PACz-FTO interactions, given the appearance of the
135 symmetric PO₃²⁻ stretching (at 996 cm⁻¹ for the control sample)^{29,30} and the disappearance of P–
136 OH vibrations¹⁴. These also indicated that solvent washing removed unbound molecules¹⁴. With
137 3-MPA addition, a redshift of approximately 5 cm⁻¹ was observed for the PO₃²⁻ vibrational mode,
138 indicating the enhanced surface binding of 2PACz – as confirmed by AIMD simulations
139 (Supplementary Note 3; Supplementary Figs. 11 and 12). ATR-FTIR of the FTO/3-MPA sample
140 (Fig. 2b) further showed carboxylate-related peaks and a reduction in the intensity of the C=O
141 peak, which correspond to the bidentate chelation of 3-MPA with FTO surfaces³¹. Combining the
142 results from XPS and ATR-FTIR, we reasoned that 3-MPA functioned as a co-adsorbent,
143 modulating the interaction of 2PACz with FTO substrates.

144 The resultant SAM uniformity was characterized by Kelvin probe force microscopy (KPFM).
145 Topography images revealed that, despite varying SAM modifications, the surface morphology of
146 FTO substrates was retained due to the ultra-thin nature of SAMs (Supplementary Fig. 13). From
147 the respective contact potential difference (CPD) maps (Fig. 2c), we recorded surface potential
148 variations on 2PACz-modified surfaces within a range of 120 mV. A Gaussian fit of the single
149 peak in the CPD distribution yielded the full-width half-maximum (FWHM) of 37 mV
150 (Supplementary Fig. 14). Introducing 3-MPA enhanced the homogeneity of electronic properties
151 on SAM-modified surfaces, as reflected by a narrower CPD distribution with the FWHM of 22
152 mV.

153 To directly visualize the distribution of SAMs on FTO substrates, we performed high-angle
154 annular dark-field (HAADF) scanning transmission electron microscopy (STEM) measurements.
155 Fig. 2d shows cross-sectional HAADF-STEM images of both control and mixed samples. Because
156 of the contrast in the atomic number², SAM was discernible as a dark layer sandwiched between
157 the brighter FTO and protective molybdenum oxide (MoO_x) layers. For the control SAM, we
158 observed thickness variations across the same FTO facet, with certain regions showing thicknesses
159 less than 1 nm. This suggests a low-density coverage and inhomogeneous distribution of 2PACz
160 molecules³². The mixed sample exhibited significant improvements in terms of SAM uniformity
161 and coverage: A consistent thickness was recorded for the mixed SAM on the same facet, albeit

162 with variations between 1 and 2 nm across different facets. Correspondingly, mixed SAM-
163 modified FTO substrates exhibited higher hydrophobicity than control SAM-modified
164 counterparts (Supplementary Fig. 15). Cyclic voltammetry (CV) measurements further determined
165 the areal density of 2PACz in the mixed SAM to be 3.9×10^{13} molecules cm^{-2} , a 70% increase
166 from the 2.3×10^{13} molecules cm^{-2} in the control SAM (Supplementary Fig. 16)^{16,27}.

167 **Characterization of perovskite films**

168 To investigate the impact of SAMs on the structural and optoelectronic properties of perovskites,
169 we fabricated triple-cation $\text{Cs}_{0.05}\text{MA}_{0.10}\text{FA}_{0.85}\text{PbI}_3$ perovskite thin films on different FTO/SAM
170 substrates. From scanning electron microscopy (SEM), we observed no notable change in the
171 perovskite surface morphology when 3-MPA was incorporated into the SAM (Fig. 3a, b). Grazing
172 incidence wide-angle x-ray scattering (GIWAXS) measurements showed nearly identical crystal
173 structures for perovskites deposited on both the control and mixed SAMs (Fig. 3c). Here, the main
174 constituent was photoactive α -phase perovskites, with traces of the 4H hexagonal phase detected
175 at $q = 0.82 \text{ \AA}^{-1}$ and 0.92 \AA^{-1} as well as PbI_2 at $q = 0.90 \text{ \AA}^{-1}$, respectively (Supplementary Fig. 14)³³.
176 Time-of-flight secondary ion mass spectrometry (TOF-SIMS) further confirmed that both 3-MPA
177 and 2PACz molecules, due to their chemisorption on FTO surfaces, remained localized at the
178 perovskite/FTO interfaces (Fig. 3d, e). These findings suggest that 3-MPA is not likely to change
179 the perovskite formation process or contribute to the grain boundary or top surface passivation.

180 We conducted photoluminescence (PL) characterization by exciting perovskite thin films at a 1-
181 sun-equivalent photon flux. We saw an average photoluminescence quantum yield (PLQY) of $0.13\% \pm 0.02\%$
182 for perovskites directly deposited onto FTO substrates, corresponding to a quasi-Fermi
183 level splitting (QFLS) of 1.105 eV (Supplementary Table 1)³⁴. 2PACz can passivate defects on
184 metal oxide surfaces and effectively block electron injection³⁵, resulting in an approximately 50-
185 fold increase in the PL intensity (Fig. 3f). We noted an average PLQY of $7\% \pm 2\%$ for the
186 perovskite/2PACz/FTO stacks (Fig. 3g), corresponding to a QFLS of 1.207 eV. The incorporation
187 of 3-MPA further improved the average PLQY to $10\% \pm 1\%$. This we ascribed to better SAM
188 coverage rather than 3-MPA passivation since the thiol group of 3-MPA was embedded within the
189 SAM (Fig. 1f).

190 We used ultraviolet and inverse photoelectron spectroscopy (UPS and IPES) to determine the work
191 function and transport energy levels of perovskites and SAMs. The secondary electron cutoff in

192 the UPS spectra indicated an increase in the work function (WF) from 4.56 to 4.93 eV upon
193 depositing the control SAM on the FTO substrate (Supplementary Fig. 18). 3-MPA led to an
194 additional WF shift of +100 meV. The ionization energy (IE) was 5.51 and 5.64 eV for the control
195 and mixed SAMs, respectively. In contrast, perovskites exhibited similar conduction band
196 minimum (CBM) and valence band maximum (VBM) on different substrates (Fig. 3h). The
197 resultant energy level diagrams of perovskites and SAMs are depicted in Fig. 3i, j. A vacuum level
198 (VL) shift of 0.17 eV was recorded between the perovskite and the 2PACz bilayer, which further
199 increased to 0.32 eV for the perovskite/mixed-SAM bilayer³⁶. A higher VL shift indicates an
200 enlarged built-in field³⁷, which in PSCs can lead to enhanced carrier extraction³⁸. Meanwhile, the
201 IE offset between the bilayer remained consistent for the control and mixed SAMs (referenced to
202 the Fermi level (E_F)).

203 **Solar cell efficiency and stability**

204 We fabricated PSCs having the inverted structure: FTO/SAM/perovskites/3,4,5-trifluoroanilinium
205 (345FAn)/fullerene (C_{60})/bathocuproine (BCP)/Ag (Fig. 4a and Supplementary Fig. 19). 345FAn
206 was selected for interface engineering due to its thermal stability¹. 2PACz (control) and 2PACz:3-
207 MPA (mixed) were employed as the SAMs for hole-selective contact. The corresponding solar
208 cell parameters are summarized in Fig. 4b. We found that compared to control devices, the mixed
209 SAM led to improved performance (average PCE 25.0% compared with 24.1%). This came from
210 open-circuit voltage (V_{oc} , from 1.141 V to 1.159 V) and fill factor (FF, from 82.3% to 84.1%)
211 (Supplementary Note 4). We noted that device reproducibility was comparable for both control
212 and mixed SAMs, likely due to SAM inhomogeneity occurring at the nanoscale^{18,27}. The champion
213 device with the mixed SAM exhibited a PCE of 25.3% from the reverse J - V scan, which agrees
214 with the PCE obtained from the steady-state power output (Supplementary Fig. 20). The integrated
215 short-circuit current density (J_{sc}) of 25.8 mA cm⁻² derived from the external quantum efficiency
216 (EQE) measurement matches well with that from the J - V sweep (Fig. 4c).

217 One mixed-SAM-based FTO device was characterized at Newport (Montana, USA); and produced
218 a QSS-certified PCE of 24.8%, with a V_{oc} of 1.150 V, a J_{sc} of 25.5 mA cm⁻², and an FF of 84.5%
219 (Fig. 4d and Supplementary Fig. 21). Although there have been reports of inverted PSCs with
220 efficiencies surpassing 25%^{2,3}, the certified PCEs measured under stabilized conditions (including
221 maximum power point (MPP) and QSS tracking) have yet to reach the same level (Supplementary

222 Table 2). The QSS efficiency reported herein represents a new record for inverted PSCs, improving
223 upon the previous record QSS efficiency of 24.09% in literature (Fig. 4e).

224 For comparison, inverted PSCs were fabricated on smooth ITO substrates. We obtained an average
225 PCE of 23.4% for control ITO devices, which was lower than that of control FTO devices, despite
226 their higher average V_{oc} and FF (Supplementary Fig. 22). This emphasizes the need to augment J_{sc}
227 for inverted PSCs. The limited J_{sc} is ascribed to the smoothness of ITO substrates (Supplementary
228 Fig. 23), leading to reduced light-scattering and thus insufficient light absorption in the full device
229 (Supplementary Fig. 24). Interestingly, the performance of mixed-SAM-based ITO devices was
230 only slightly improved, possibly due to the weak interactions of 3-MPA with ITO surfaces
231 (Supplementary Note 5; Supplementary Fig. 25).

232 We evaluated the operating stability of PSCs using International Summit on Organic Photovoltaic
233 Stability (ISOS)-L-3 protocols, in which the encapsulated device was subjected to continuous 1-
234 sun equivalent, white-LED illumination (Supplementary Fig. 26) at 50% relative humidity and
235 heatsink temperature of 65°C. To impede ion and moisture diffusion, we replaced BCP with
236 atomic-layer-deposited SnO₂ as a buffer layer⁹. The resultant device delivered a PCE of 24.6% at
237 room temperature (Supplementary Fig. 27). During the ISOS-L-3 testing, the device initially
238 demonstrated a PCE of 22.6%, which increased to 23.1% after 1.6 hours of MPP tracking (Fig. 4f).
239 The lower PCE at 65°C, compared to room temperature, is ascribed to the negative temperature
240 coefficient of PSCs ($-0.15\%/^{\circ}\text{C}$)³⁹. The PCE stabilized at 21.9% (95% of the peak PCE) until the
241 end of the test (1075 h), with the main degradation in the photocurrent (Supplementary Fig. 28).
242 The initial performance and operating stability reported herein are compared with other PSCs
243 subjected to ISOS-L-3 tests (Supplementary Table 3).

244 References

- 245 1. Park, S. M. *et al.* Engineering ligand reactivity enables high-temperature operation of
246 stable perovskite solar cells. *Science* **381**, 209–215 (2023).
- 247 2. Zhang, S. *et al.* Minimizing buried interfacial defects for efficient inverted perovskite solar
248 cells. *Science* **380**, 404–409 (2023).
- 249 3. Jiang, Q. *et al.* Surface reaction for efficient and stable inverted perovskite solar cells.
250 *Nature* **611**, 278–283 (2022).
- 251 4. Kim, M. *et al.* Conformal quantum dot–SnO₂ layers as electron transporters for efficient
252 perovskite solar cells. *Science* **375**, 302–306 (2022).

- 253 5. Park, J. *et al.* Controlled growth of perovskite layers with volatile alkylammonium chlorides.
254 *Nature* **616**, 724–730 (2023).
- 255 6. Best Research-Cell Efficiency Chart. *NREL* <https://www.nrel.gov/pv/cell-efficiency.html>
256 (2023).
- 257 7. You, S. *et al.* Radical polymeric p-doping and grain modulation for stable, efficient
258 perovskite solar modules. *Science* **379**, 288–294 (2023).
- 259 8. Zheng, X. *et al.* Managing grains and interfaces via ligand anchoring enables 22.3%-
260 efficiency inverted perovskite solar cells. *Nat. Energy* **5**, 131–140 (2020).
- 261 9. Chen, H. *et al.* Quantum-size-tuned heterostructures enable efficient and stable inverted
262 perovskite solar cells. *Nat. Photonics* **16**, 352–358 (2022).
- 263 10. Li, Z. *et al.* Organometallic-functionalized interfaces for highly efficient inverted perovskite
264 solar cells. *Science* **376**, 416–420 (2022).
- 265 11. Peng, W. *et al.* Reducing nonradiative recombination in perovskite solar cells with a porous
266 insulator contact. *Science* **379**, 683–690 (2023).
- 267 12. Camaioni, N. *et al.* Polymer solar cells with active layer thickness compatible with scalable
268 fabrication processes: a meta-analysis. *Adv. Mater.* **35**, 2210146 (2023).
- 269 13. Sahli, F. *et al.* Fully textured monolithic perovskite/silicon tandem solar cells with 25.2%
270 power conversion efficiency. *Nat. Mater.* **17**, 820–826 (2018).
- 271 14. Al-Ashouri, A. *et al.* Conformal monolayer contacts with lossless interfaces for perovskite
272 single junction and monolithic tandem solar cells. *Energy. Environ. Sci.* **12**, 3356–3369
273 (2019).
- 274 15. Paniagua, S. A. *et al.* Phosphonic acids for interfacial engineering of transparent conductive
275 oxides. *Chem. Rev.* **116**, 7117–7158 (2016).
- 276 16. Truong, M. A. *et al.* Tripodal triazatruxene derivative as a face-on oriented hole-collecting
277 monolayer for efficient and stable inverted perovskite solar cells. *J. Am. Chem. Soc.* **145**,
278 7528–7539 (2023).
- 279 17. Isikgor, F. H. *et al.* Molecular engineering of contact interfaces for high-performance
280 perovskite solar cells. *Nat. Rev. Mater.* **8**, 89–108 (2022).
- 281 18. Mao, L. *et al.* Fully textured, production-line compatible monolithic perovskite/silicon
282 tandem solar cells approaching 29% efficiency. *Adv. Mater.* **34**, 1–12 (2022).
- 283 19. He, R. *et al.* Improving interface quality for 1-cm² all-perovskite tandem solar cells. *Nature*
284 **618**, 80–86 (2023).
- 285 20. Phung, N. *et al.* Enhanced self-assembled monolayer surface coverage by ALD NiO in p-i-
286 n perovskite solar cells. *ACS Appl. Mater. Interfaces* **14**, 2166–2176 (2022).
- 287 21. Farag, A. *et al.* Evaporated self-assembled monolayer hole transport layers: lossless
288 interfaces in p-i-n perovskite solar cells. *Adv. Energy Mater.* **13**, 2203982 (2023).

- 289 22. Boyd, C. C. *et al.* Overcoming redox reactions at perovskite-nickel oxide interfaces to boost
290 voltages in perovskite solar cells. *Joule* **4**, 1759–1775 (2020).
- 291 23. Fukano, T. Low-temperature growth of highly crystallized transparent conductive fluorine-
292 doped tin oxide films by intermittent spray pyrolysis deposition. *Sol. Energy Mater Sol.*
293 *Cells* **82**, 567–575 (2004).
- 294 24. Neale, N. R., Kopidakis, N., van de Lagemaat, J., Grätzel, M. & Frank, A. J. Effect of a
295 coadsorbent on the performance of dye-sensitized tio₂ solar cells: shielding versus band-
296 edge movement. *J. Phys. Chem. B* **109**, 23183–23189 (2005).
- 297 25. Deng, X. *et al.* Co-assembled monolayers as hole-selective contact for high-performance
298 inverted perovskite solar cells with optimized recombination loss and long-term stability.
299 *Angew. Chem. Int. Ed.* **134**, (2022).
- 300 26. Al-Ashouri, A. *et al.* Wettability improvement of a carbazole-based hole-selective
301 monolayer for reproducible perovskite solar cells. *ACS Energy Lett.* **8**, 898–900 (2023).
- 302 27. Liu, M. *et al.* Compact hole-selective self-assembled monolayers enabled by disassembling
303 micelles in solution for efficient perovskite solar cells. *Adv. Mater.* (2023)
304 doi:10.1002/adma.202304415.
- 305 28. Love, J. C., Estroff, L. A., Kriebel, J. K., Nuzzo, R. G. & Whitesides, G. M. Self-assembled
306 monolayers of thiolates on metals as a form of nanotechnology. *Chem. Rev.* **105**, 1103–
307 1170 (2005).
- 308 29. Paniagua, S. A. *et al.* Phosphonic acid modification of indium–tin oxide electrodes:
309 combined XPS/UPS/contact angle studies. *J. Phys. Chem. C* **112**, 7809–7817 (2008).
- 310 30. Hotchkiss, P. J., Malicki, M., Giordano, A. J., Armstrong, N. R. & Marder, S. R.
311 Characterization of phosphonic acid binding to zinc oxide. *J. Mater. Chem.* **21**, 3107 (2011).
- 312 31. Nazeeruddin, M. K., Humphry-Baker, R., Liska, P. & Grätzel, M. Investigation of sensitizer
313 adsorption and the influence of protons on current and voltage of a dye-sensitized
314 nanocrystalline TiO₂ solar cell. *J. Phys. Chem. B* **107**, 8981–8987 (2003).
- 315 32. Bunker, B. C. *et al.* The impact of solution agglomeration on the deposition of self-
316 assembled monolayers. *Langmuir* **16**, 7742–7751 (2000).
- 317 33. Dang, H. X. *et al.* Multi-cation synergy suppresses phase segregation in mixed-halide
318 perovskites. *Joule* **3**, 1746–1764 (2019).
- 319 34. Caprioglio, P. *et al.* On the relation between the open-circuit voltage and quasi-fermi level
320 splitting in efficient perovskite solar cells. *Adv. Energy Mater.* **9**, 1901631 (2019).
- 321 35. Al-Ashouri, A. *et al.* Monolithic perovskite/silicon tandem solar cell with >29% efficiency
322 by enhanced hole extraction. *Science* **370**, 1300–1309 (2020).
- 323 36. Li, X. *et al.* Mapping the energy level alignment at donor/acceptor interfaces in non-
324 fullerene organic solar cells. *Nat. Commun.* **13**, 2046 (2022).
- 325 37. Lami, V. *et al.* Visualizing the vertical energetic landscape in organic photovoltaics. *Joule*
326 **3**, 2513–2534 (2019).

- 327 38. Sandberg, O. J. *et al.* On the question of the need for a built-in potential in perovskite solar
328 cells. *Adv. Mater. Interfaces* **7**, 2000041 (2020).
- 329 39. Moot, T. *et al.* Temperature coefficients of perovskite photovoltaics for energy yield
330 calculations. *ACS Energy Lett.* **6**, 2038–2047 (2021).

ACCELERATED ARTICLE PREVIEW

331 **Figure Legends**

332 **Fig.1|MD simulations of phosphonic acid adsorption with and without molecular additives.**
333 **a**, Chemical structures of the phosphonic acid 2PACz and the bifunctional compound 3-MPA. **b**,
334 Total number of 2PACz clusters formed over a set period, in the absence (control) and presence
335 (mixed) of 3-MPA. **c**, Types of 2PACz clusters formed at equilibrium. **d**, **e**, Top views of
336 equilibrated molecular representations of control (**d**) and mixed (**e**) systems. 2PACz and 3-MPA
337 (where applicable) are shown in pink and blue, respectively; Sn and O atoms, shown in the
338 background, are depicted in yellow and red, respectively. **f**, Successive steps along an AIMD
339 trajectory showcasing the role of 3-MPA as a co-adsorbent. Large, encircled areas are
340 magnifications of small ones.

341 **Fig.2|Homogeneity of self-assembled monolayers formed on FTO substrates.** **a**, XPS P 2*p* (left)
342 and S 2*p* (right) spectra for the control and mixed samples. The peaks were fitted using one S 2*p*
343 or P 2*p* doublet with a 2:1 peak area ratio. **b**, 2PACz (left) and 3-MPA (right) transmission FTIR
344 spectra, compared with ATR-FTIR spectra for the SAM (left) and 3-MPA (right) coated FTO
345 substrates. The FTIR peaks identified at 947 and 1021 cm⁻¹ for 2PACz powders correspond to the
346 symmetric and asymmetric stretching of P–OH, respectively. Cz = carbazole. **c**, KPFM images of
347 control (left) and mixed (right) SAM-coated FTO substrates. **d**, Cross-sectional HAADF-STEM
348 images of control (top) and mixed (bottom) SAMs sandwiched between MoO_x and FTO.

349 **Fig.3|Materials properties of perovskite films on different FTO/SAM substrates.** **a**, **b**, Top-
350 view SEM images of perovskite films deposited on control (**a**) and mixed (**b**) SAMs. **c**, GIWAXS
351 images for perovskite films on control (left) and mixed (right) SAMs. The color bar shows the
352 diffraction intensity collected from the GIWAXS detector. q_{xy} and q_z represent in-plane and near
353 out-of-plane scattering vectors, respectively. **d**, **e**, TOF-SIMS profiles of perovskites on
354 FTO/control SAM (**d**) and FTO/mixed SAM (**e**) substrates measured in negative polarity. Traces
355 of SH⁻ were identified at the perovskite/control SAM interface, possibly due to contamination of
356 precursor materials. **f**, Absolute intensity PL spectra of perovskite films on bare FTO (no SAM)
357 and control and mixed SAMs. **g**, PLQYs of perovskite films on control and mixed SAMs (5
358 samples for each condition). Statistical distribution represented in box plots (line within the box:
359 mean, box limit: standard deviation). **h**, UPS and IPES spectra of perovskite films on control and
360 mixed SAMs. Gaussian fit (grey line) was used to determine the conduction and valence bands. **i**,
361 **j**, Schematic energy level diagrams of the perovskite/control SAM (**i**) and perovskite/mixed SAM
362 bilayer (**j**), respectively.

363 **Fig.4|Photovoltaic performance of perovskites solar cells.** **a**, Schematic illustration of the
364 device architecture with textured FTO substrate. **b**, Solar cell parameters for the control (16 devices)
365 and mixed (32 devices) SAM devices. Statistical distribution represented in box-and-whisker plots
366 (line within box: median, box limit: standard deviation, whiskers: 1.5 outliers). **c**, EQE and
367 integrated J_{sc} (grey dashed line) curves of the mixed SAM device. **d**, QSS J - V curve of one
368 representative mixed SAM device certified at Newport. Inset: PV parameters of the device. **e**,
369 Certified performance of inverted PSCs measured under the QSS condition. **f**, MPP tracking of the
370 encapsulated mixed SAM device at heatsink temperature of 65°C with a relative humidity of ~50%
371 under 1-sun illumination. The device configuration is FTO/SAM/Perovskite/345FAn/C₆₀/ALD-
372 SnO₂/Ag, having a PCE of 24.6% at room temperature.

373 **Methods**

374 **Molecular dynamics simulations**

375 Static DFT calculation and AIMD were performed with the CP2K⁴⁰ package utilizing a mixed
376 Gaussian/plane wave (GPW) basis. The PBE exchange-correlation functional⁴¹, DFT-D3
377 dispersion corrections⁴², and dipole corrections⁴³ necessary for periodic boundary conditions along
378 the perpendicular direction to the surface were included. Valence electron wave functions were
379 expanded in a double- ζ Gaussian basis set with polarization functions (DZVP)⁴⁴. The energy cut-
380 off for the electron density expansion in the GPW method was 400 Ry. Born-Oppenheimer AIMD
381 simulations were run with an integration time step of 0.5 fs and the system was kept at 300 K using
382 the thermostat of Bussi et al.⁴⁵ in a canonical isothermal-isochoric (NVT) ensemble, where the
383 total number of atoms N , the volume V and the temperature T of the system were held constant.
384 All AIMD simulations were performed at Γ point. Being the most stable surface, the SnO₂ (110)
385 was chosen as the substrate surface. The systems were equilibrated over 5 ps in the NVT ensemble
386 and the remaining 40 ps were used for the production run. To investigate the interactions between
387 the 2PACz and 3-MPA molecules, as well as molecules and the SnO₂ substrate, 5 scenarios were
388 simulated: (1) a single molecule (2PCAz or 3-MPA) on SnO₂ (110), (2) one 2PACz and one 3-
389 MPA concurrently on SnO₂ (110), (3) two 2PACz and one 3-MPA on SnO₂(110), (4) four 2PACz
390 and one 3-MPA on SnO₂(110), and (5) six 2PACz and one 3-MPA on SnO₂ (110). In all the
391 scenarios, an in-plane SnO₂ (110) simulation cell of 22.690 Å × 27.756 Å with 45 Å of vacuum
392 between the slab repetitions was used. AIMD was also used to estimate the interaction energy of
393 2PACz and 3-MPA with the SnO₂ (110) surface. The final AIMD configurations were relaxed with
394 DFT to extract the interaction energies of the molecules. Binding energies were calculated as
395 $\Delta E_b = E_{\text{tot}} - E_s - E_{\text{mol}}$, where E_{tot} is the energy of the final relaxed configuration (molecule on
396 SnO₂ (110)); E_s is the energy of the final configuration of the slab; E_{mol} is the energy of the final
397 configuration of the isolated molecule. The interaction energies of 2PACz clusters were computed
398 after DFT relaxations of isolated clusters. Dimers, trimers, and tetramers were considered.
399 Interaction energies per molecule were calculated as $\Delta E_i = (E_{\text{tot}} - nE_{\text{mol}})/n$, where E_{tot} is the energy
400 of the final relaxed cluster; n is the number of molecules forming the cluster; E_{mol} is the energy of
401 a single relaxed molecule assumed isolated. Vibrational power spectra were computed as the
402 Fourier transform of the autocorrelation function of the atomic velocities.

403 Classical MD simulations with full atomic resolution were realized with the help of the LAMMPS
404 MD simulator⁴⁶. The equations of motion were integrated using the Velocity-Verlet method⁴⁷, with
405 a 1 fs time step, while bond stretching was not constrained for any bonds. To maintain isothermal
406 conditions, the deterministic Nosé – Hoover thermostat^{48,49}, with a time constant equal to 0.1 ps,
407 was utilized. This ensured that thermostating was applied to both translational and rotational
408 degrees of freedom, crucial for the asymmetric 2PACz and 3-MPA molecules. All classical MD
409 simulations were realized in the canonical NVT ensemble at $T = 300\text{K}$ comprising a V-shaped
410 SnO₂ (110) model system with dimensions 60 Å × 105 Å × 40 Å. Periodic boundary conditions
411 were used in x- and y-directions, whereas reflective boundary conditions were employed in the z-
412 direction. The two considered systems, control and mixed, comprised a total of 18498 and 18714
413 atoms, respectively, whereas the experimental molar ratio (2PACz/3-MPA= 9/1) was retained in
414 the simulated mixed system. The systems were equilibrated for 1 ns followed by a 10ns production
415 simulation, where sampling took place every 500 fs for the calculation of ensemble averages. A
416 snapshot of the system was taken every 1000 fs for visualization purposes. The calculation of the
417 number distributions of formed 2PACz clusters was performed through an in-house code utilizing

418 a threshold distance of 8 Å among the centre of masses of adjacent 2PACz molecules in accordance
419 with the nearest neighbour shell of the corresponding radial distribution function as clustering
420 criterion.

421 To accurately capture the interactions of SnO₂, the thoroughly validated classical force field
422 developed by Bandura et al.⁵⁰ was used. The all-atom OPLS force field was utilized for 3-MPA,
423 wherein the corresponding interaction parameters were obtained with the help of the LigParGen
424 server⁵¹. For 2PACz, containing the phosphonic functional group, the specially designed force field
425 developed by Meltzer et al.⁵² based on the Generalized Amber Force Field⁵³ was utilized. The van
426 der Waals and electrostatic non-bonded interactions were calculated using a real-space cutoff
427 radius of 10 Å and 8 Å, respectively, whereas the particle-particle-particle-mesh (PPPM) scheme⁵⁴
428 with an accuracy of 0.0001 (kcal/mol)/Å was used for the consideration of long-range electrostatic
429 interactions. Because the SnO₂ force field uses a Buckingham potential for the van der Waals
430 interactions, its combination with the Lennard-Jones potential used for the compounds was
431 realized by fitting the Buckingham parameters of SnO₂ to a suitable set of Lennard-Jones
432 parameters⁵⁵ and geometric mixing rules were applied for all dissimilar non-bonded interactions.

433 **Materials**

434 All materials were used as received without further purification. Organic halide salts, including
435 methylammonium iodide (MAI), formamidinium iodide (FAI), methylammonium chloride
436 (MACl), were purchased from Great Cell Solar. Cesium iodide (CsI), 3-mercaptopropionic acid
437 (3-MPA), 3,4,5-trifluoroaniline (98%), and guanidinium thiocyanate (GuaSCN) were purchased
438 from Sigma-Aldrich. 3,4,5-trifluoroaniline was converted to its ammonium form following the
439 published procedure. [2-(9H-Carbazol-9-yl)ethyl]phosphonic Acid (2PACz), lead iodide (PbI₂,
440 99.99%), and bathocuproine (BCP) were purchased from TCI. Anhydrous solvents including N,
441 N-dimethylformamide (DMF, 99.8%), dimethyl sulfoxide (DMSO, 99.9%), 2-propanol (IPA,
442 99.5%), chloroform (CF, 99.8%), and anisole (99.7%) were purchased from Sigma-Aldrich. C₆₀
443 was purchased from Xi'an Polymer Light Technology Corp. ITO and FTO (TEC 10) substrates
444 were purchased from Thin Film Devices Inc. and Ossila, respectively.

445 **Perovskite film fabrication**

446 1.5 M of Cs_{0.05}MA_{0.1}FA_{0.85}PbI₃ perovskite precursor was fully dissolved in mixed solvents of DMF
447 and DMSO (4:1, v/v) with the molar ratio for FAI/MAI/CsI was 0.85:0.1:0.05. 10 mg mL⁻¹ MACl
448 and 8 mg mL⁻¹ GuaSCN were added in the solution to improve the film morphology. The precursor
449 solution was filtered through a 0.22 μm polytetrafluoroethylene (PTFE) membrane before use. 60
450 μL of perovskite solution was deposited on the substrate and spun cast at 1000 rpm for 10 s
451 followed by 6000 rpm for 30 s. 150 μL anisole was dropped onto the substrate during the last 5 s
452 of the spinning, resulting in the formation of dark brown films that were then annealed on a hot
453 plate at 100°C for ITO and 120°C for FTO for 20 min.

454 **Device fabrication**

455 FTO glasses were sequentially sonicated in aqueous detergent, deionized water, acetone, and IPA
456 each for 10 min. After drying with nitrogen, the substrates were exposed to UV-ozone treatment
457 for 15 min to remove organic contaminants and then transferred into a nitrogen-filled glovebox
458 maintaining less than 0.1 ppm of O₂ and H₂O. 100 μL of 2PACz or a mixture of 2PACz:3-MPA (in
459 a molar ratio of either 9:1 in characterization and device fabrication, or 8:2 in XPS measurements)

460 in anhydrous ethanol (1 mM) solution was uniformly spread on the substrates and allowed to rest
461 for 15 s, followed by spinning the films at 3000 rpm for 30s. The films were then annealed at
462 100°C for 10 min and washed by dropping 500 μL ethanol during the film spinning at 3000 rpm.
463 Perovskites solution was deposited on the SAM-modified substrate as detailed above. 200 μL of
464 345FAn solution (1 mg/mL) in CF with an additional 3% of IPA was then drop cast within 2-3 s
465 on the perovskite film spinning at 4000 rpm (i.e., dynamic spinning) and annealed at 100°C for 5
466 min. Both control and mixed SAM films were then transferred to the thermal evaporator
467 (Angstrom engineering). C_{60} (30 nm) and BCP (7 nm) were deposited sequentially with a rate of
468 0.3 \AA s^{-1} and 0.5 \AA s^{-1} , respectively, at a pressure of ca. 2×10^{-6} mbar. Finally, Ag contact (140
469 nm) was deposited on top of BCP through a shadow mask with the desired aperture area. For the
470 stability testing, ALD- SnO_2 were used as the barrier layer. The deposition of ALD- SnO_2 was
471 carried out in the PICOSUN R-200 Advanced ALD system. H_2O and TDMASn were used as
472 oxygen and tin precursors. Precursor and substrate temperature were set to 75°C and 85°C,
473 respectively. 90 SCCM N_2 was used as carrier gas. Pulse and purge times for H_2O were 1 s and 5
474 s, and 1.6 s and 5 s for TDMASn . The total deposition cycle is 120, corresponding to 20 nm of
475 SnO_2 .

476 **Solar cell characterization**

477 The current-voltage (I - V) characteristics of solar cells were measured using a Keithley 2400
478 sourcemeter under the illumination of solar simulator (Newport, Class AAA) at the light intensity
479 of 100 mW cm^{-2} as checked with a calibrated reference solar cell (Newport). The stabilized PCE
480 was measured by setting the bias voltage to the V_{MPP} and then tracing the current density. The V_{MPP}
481 was determined from the reverse I - V curve. The active area was determined by the aperture shade
482 mask (0.049 cm^2) placed in front of the solar cell to avoid overestimation of the photocurrent
483 density. EQE spectra were recorded with a commercial system (Arkeo-Ariadne, Cicci Research
484 s.r.l.) based on a 300 W xenon light source and a holographic grating monochromator (Cornerstone,
485 Newport).

486 **Stability tests of solar cells**

487 Devices were placed in a homemade stability tracking station. The illumination source is a white
488 light LED with intensity calibrated to match the 1-sun condition. For the ISOS-L-3 ageing protocol
489 (65 or 85°C ; 50% relative humidity; MPP)⁵⁶, the device chamber was left open in a room with
490 $50 \pm 10\%$ humidity and solar cell was mounted on a metal plate kept at 65°C by a heating element.
491 A thermal couple attached to the metal plate was used to monitor and provide feedback control to
492 the heating element to ensure temperature consistency. MPP was tracked using a home-build
493 MATLAB-based MPP tracking system using a 'perturb and observe' method. The MPP was
494 updated every 1000 minutes. Encapsulation was done by capping the device with a glass slide,
495 using UV-adhesive (Lumtec LT-U001) as a sealant.

496 **XPS measurements**

497 XPS measurements were performed with a Thermo Scientific K-Alpha system with 180° double-
498 focusing, hemispherical analyser. The system is equipped with a 128-channel detector and
499 monochromatic small spot XPS. An Al $\text{K}\alpha$ source (1486.6 eV) was used for excitation and a pass
500 energy of 50 eV was used for XPS acquisition. Samples mounted on a metal specimen holder. All
501 data were analysed with CasaXPS and Thermo Avantage software.

502 **KPFM measurements**

503 KPFM measurements were performed using an Asylum Research Cypher S atomic force
504 microscope (Oxford Instruments, Santa Barbara, USA) with an ASYELEC.01-R2 Ti-Ir coated
505 cantilever (Asylum Research). Scans were performed over 2 μm at 512 pixels and 0.5 Hz using a
506 two-pass method where the first pass is a tapping mode topography scan and the second in KPFM
507 mode with a tip potential of 3 V and a surface clearance of 5 nm. Cantilever calibration was
508 performed using the Thermal method from the Asylum Research GetReal database.

509 **HAADF-TEM measurements**

510 HAADF-TEM images were acquired at an aberration corrected FEI (Titan Cubed Themis G2)
511 operated at 300 kV equipped with an XFEG gun and Bruker Super-X EDS detectors. The SAM
512 samples had a structure of glass/FTO/SAM/MoO_x (50 nm), where the MoO_x layer was deposited
513 through thermal evaporation with a low rate of 0.1 \AA s^{-1} at a pressure below 2×10^{-4} Pa. The cross-
514 sectional samples were prepared by using a focused ion beam system (FIB, Helios G4 UX).
515 Another protective layer of carbon was thermally evaporated before ion-beam cutting and etching.

516 **CV measurements**

517 CV measurements were conducted using a three-electrode configuration with a potentiostat
518 (PGSTAT204, Autolab). The working electrodes were prepared using a spin coating method on
519 an FTO electrode. The exposed area of the working electrode to the electrolyte measures 8 mm \times
520 21.4 mm. A platinum plate and an Ag/AgCl electrode (in a 3.0 M KCl solution) were employed
521 as the counter and reference electrodes, respectively. The measurements were performed in an Ar-
522 saturated solution of 1,2-dichlorobenzene (o-DCB) with 0.1 M tetrabutylammonium
523 hexafluorophosphate (TBA⁺PF₆⁻) serving as the supporting electrolyte. All potentials are
524 referenced against the ferrocene redox couple, serving as an internal standard. The effective
525 coverage of the self-assembled monolayers on the FTO surface is measured by the slope of a linear
526 dependency of the oxidative peak intensity against the scan rate as follows:

$$527 \quad i_{p,o} = \frac{n^2 F^2}{4RTN_A} A I^* v$$

528 $i_{p,o}$ is the oxidative peak current, v is the voltage scan rate, n is the number of electrons transferred,
529 F is the Faraday constant (96,485 C mol⁻¹), R is the universal gas constant (8.314 J K⁻¹ mol⁻¹), T
530 is the temperature, N_A is the Avogadro constant, A is the electrode area, and I^* is the areal density.

531 **UPS and IPES measurements**

532 UPS measurements were taken with an Excitech H Lyman- α photon source (10.2 eV) with a
533 nitrogen-filled beam path coupled with a PHI 5600 UHV and analyser system. A sample bias of -
534 5 V was applied and a pass energy of 5.85 eV was used for UPS acquisition. IPES measurements
535 were performed in the Bremsstrahlung isochromatic mode with electron kinetic energies below 5
536 eV and an electron gun emission current of 2 μA was used to minimize sample damage. A Kimball
537 Physics ELG-2 electron gun with a BaO cathode was used to generate the electron beam. Emitted
538 photons were collected with a bandpass photon detector consisting of an optical bandpass filter
539 (254 nm, Semrock) and a photomultiplier tube (R585, Hamamatsu Photonics). Samples were held
540 at a -20 V bias during all IPES measurements and the UHV chamber was completely dark.

541 **Other characterizations**

542 Particle size distributions in solutions were determined by the DLS technique using a Malvern
543 Zetasizer Nano ZS. Contact angles were measured using VCA-Optima XE. The image was taken
544 with CCD camera within 1 s after water droplet. GIWAXS measurements were performed at CMS
545 beamline, NSLS II. The monochromatic X-ray with the energy of 13.5 keV shone upon the
546 samples at different grazing incident angles of 1°, 0.5°, and 0.08° with an exposure time of 10 s.
547 A Pilatus800K detector was placed 259 mm away from the sample to capture the 2D diffraction
548 pattern. Absolute intensity photoluminescence spectra were measured using an integrating sphere,
549 and Andor Kymera 193i spectrograph, and a 660 nm continuous-wave laser set at 1-sun equivalent
550 photon flux (1.1 μm beam full-width half-maximum, 632 μW); photoluminescence was collected
551 at normal incidence using a 0.1 NA, 110 μm-diameter optical fiber. TOF-SIMS was conducted on
552 the IONTOF M6 instrument with a Bi³⁺ (30 keV) primary ion beam for analysis and an Cs-cluster
553 gun (2 keV) for sputtering. Data was acquired in positive mode with an analysis area of 49 × 49
554 μm² centred and a raster area of 200 × 200 μm². IR spectra were obtained in the attenuated total
555 reflectance mode using a Fourier-transform IR spectrometer (Thermo Scientific iS50). Samples
556 were prepared on the FTO substrate and scanned in the spectral range of 4000 to 550 cm⁻¹ with a
557 minimum number of 500 scans and a resolution of 4 cm⁻¹. The triangular apodization function was
558 used to improve the signal-to-noise ratio. High-resolution SEM images were obtained using the
559 Hitachi S5200 microscope with an accelerating voltage of 1.5 kV. A low accelerating voltage and
560 a low beam current were deployed to reduce surface damage of perovskite films under electron
561 beam bombardment. The diffuse and specular light reflected from the substrate surface was
562 measured using a Cary 5000 UV-Vis-NIR double-beam spectrophotometer in diffuse reflectance
563 mode. Pure BaSO₄ was used for the baseline collection.

564 **Additional References**

- 565 40. Kühne, T. D. *et al.* CP2K: An electronic structure and molecular dynamics software package
566 - Quickstep: Efficient and accurate electronic structure calculations. *J. Chem. Phys.* **152**,
567 194103 (2020).
- 568 41. Van Setten, M. J. *et al.* The PseudoDojo: Training and grading a 85 element optimized
569 norm-conserving pseudopotential table. *Comput. Phys. Commun.* **226**, 39–54 (2018).
- 570 42. Grimme, S. Density functional theory with London dispersion corrections. *Wiley Interdiscip.*
571 *Rev. Comput. Mol. Sci.* **1**, 211–228 (2011).
- 572 43. Bengtsson, L. Dipole correction for surface supercell calculations. *Phys. Rev. B* **59**, 12301–
573 12304 (1999).
- 574 44. VandeVondele, J. & Hutter, J. Gaussian basis sets for accurate calculations on molecular
575 systems in gas and condensed phases. *J. Chem. Phys.* **127**, 114105 (2007).
- 576 45. Bussi, G., Donadio, D. & Parrinello, M. Canonical sampling through velocity rescaling. *J.*
577 *Chem. Phys.* **126**, 014101 (2007).
- 578 46. Kryuchkov, N. P., Yurchenko, S. O., Fomin, Y. D., Tsiok, E. N. & Ryzhov, V. N. Complex
579 crystalline structures in a two-dimensional core-softened system. *Soft Matter.* **14**, 2152–
580 2162 (2018).

- 581 47. Swope, W. C., Andersen, H. C., Berens, P. H. & Wilson, K. R. A computer simulation
582 method for the calculation of equilibrium constants for the formation of physical clusters of
583 molecules: Application to small water clusters. *J. Chem. Phys.* **76**, 637–649 (1982).
- 584 48. Nosé, S. A unified formulation of the constant temperature molecular dynamics methods. *J.*
585 *Chem. Phys.* **81**, 511–519 (1984).
- 586 49. Kassir, Y., Kupiec, M., Shalom, A. & Simchen, G. Cloning and mapping of CDC40, a
587 *Saccharomyces cerevisiae* gene with a role in DNA repair. *Curr. Genet.* **9**, 253–257 (1985).
- 588 50. Bandura, A. V., Sofo, J. O. & Kubicki, J. D. derivation of force field parameters for SnO₂
589 –H₂O surface systems from plane-wave density functional theory calculations. *J. Phys.*
590 *Chem. B* **110**, 8386–8397 (2006).
- 591 51. Dodda, L. S., Cabeza de Vaca, I., Tirado-Rives, J. & Jorgensen, W. L. LigParGen web
592 server: an automatic OPLS-AA parameter generator for organic ligands. *Nucleic Acids Res.*
593 **45**, W331–W336 (2017).
- 594 52. Meltzer, C. *et al.* indentation and self-healing mechanisms of a self-assembled monolayer—
595 a combined experimental and modeling study. *J. Am. Chem. Soc.* **136**, 10718–10727 (2014).
- 596 53. Wang, J., Wolf, R. M., Caldwell, J. W., Kollman, P. A. & Case, D. A. Development and
597 testing of a general amber force field. *J. Comput. Chem.* **25**, 1157–1174 (2004).
- 598 54. Hockney, R. W. & Eastwood, J. W. *Computer Simulation Using Particles*. (CRC Press,
599 2021). doi:10.1201/9780367806934.
- 600 55. Lim, T.-C. Alignment of Buckingham parameters to generalized Lennard-Jones potential
601 functions. *Zeitschrift für Naturforschung A* **64**, 200–204 (2009).
- 602 56. Khenkin, M. V. *et al.* Consensus statement for stability assessment and reporting for
603 perovskite photovoltaics based on ISOS procedures. *Nat. Energy* **5**, 35–49 (2020).

604

605 Acknowledgements

606 This research was made possible by the U.S. Department of the Navy, Office of Naval Research
607 Grant (N00014-20-1-2572). This work was supported in part by Ontario Research Fund-Research
608 Excellence program (ORF7-Ministry of Research and Innovation, Ontario Research Fund-
609 Research Excellence Round 7). This work was also supported under award number OSR-
610 CRG2020-4350.2. M.W. acknowledges funding from the European Union’s Horizon 2020
611 Research and Innovation program under the Marie Skłodowska-Curie Grant Agreement No.
612 101026353. T.H., H.R.A., and K.R.G. gratefully acknowledge funding from the National Science
613 Foundation under award no. DMR-2102257. L.X. acknowledges support by National Natural
614 Science Foundation of China (no. 61935016, 52173153) and the Electron Microscopy Laboratory
615 of Peking University for the use of electron microscopes. M.G.K. acknowledges support by the

616 Office of Naval Research under award number N00014-20-1-2725. A.A. acknowledges support
617 by the Office of Naval Research under award number N00014-20-1-2573. P.S. acknowledges the
618 support of the Vanier Canada Graduate Scholarship. This work made use of the NUFAB and Keck-
619 II facilities of Northwestern University's NUANCE Center, which has received support from the
620 SHyNE Resource (NSF ECCS-2025633), the IIN, and Northwestern's MRSEC program (NSF
621 DMR-1720139). We thank Damir Kopilovic for providing the LED spectrum and Jing Gao for
622 assisting with the SEM measurements.

623 **Author contributions**

624 S.M.P., M.W., M.G., and E.H.S. conceived the idea and proposed the experimental and modelling
625 design. N.L., L.A., V.C., and U.R. carried out the MD simulation. S.M.P. fabricated all the devices
626 and conducted the characterization. T.H., H.R.A and K.R.G performed XPS, UPS, and IPES
627 characterization and data analysis. W.Y. and L.X. carried out the HAADF-STEM measurements.
628 F.T.E., M.W., S.M.Z., and M.G. conducted the PL and EQE characterization and data analysis.
629 M.W. measured DLS. H.S. conducted CV measurements and data analysis. D.C. performed UV-
630 Vis spectroscopy characterization. Y.Y. and M.G.K. measured TOF-SIMS. K.D. and A.A.
631 performed the GIWAXS measurements. M.V., E.D.J. and D.B.K. helped with the device
632 fabrication and material characterization. P.S. and T.F. performed the KPFM measurements. M.W.,
633 S.M.P., N.L., M.G., and E.H.S. co-wrote the manuscript. All authors contributed to data analysis,
634 read, and commented on the manuscript.

635 **Competing interests**

636 The authors declare no competing interests.

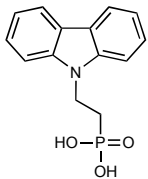
637 **Data availability**

638 All data are available in the main text or the supplementary materials. Further data are available
639 from the corresponding author on reasonable request.

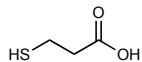
640 **Code availability**

641 The codes and post-analysis tools for MD simulations are available in the following repository:
642 <https://doi.org/10.5281/zenodo.8393081>.

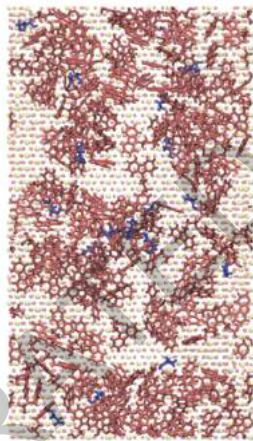
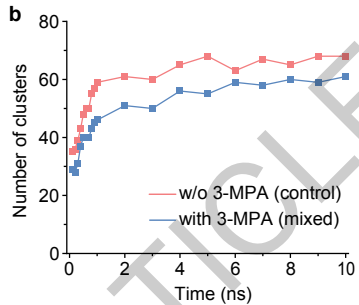
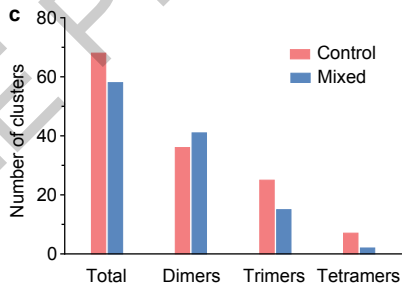
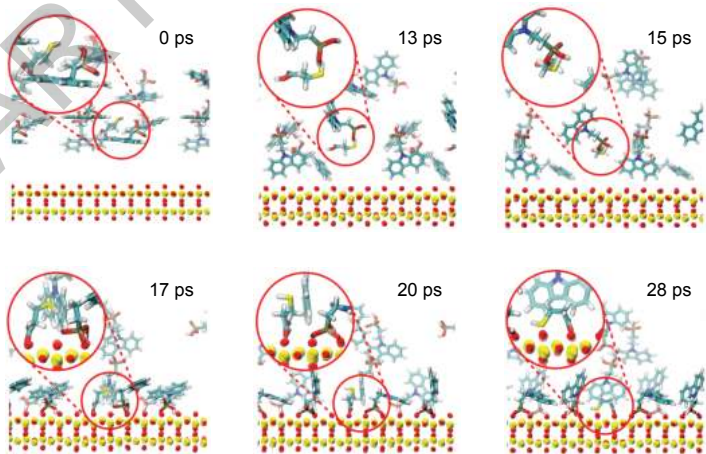
643 **Correspondence and requests for materials** should be addressed to M.G. or E.H.S.

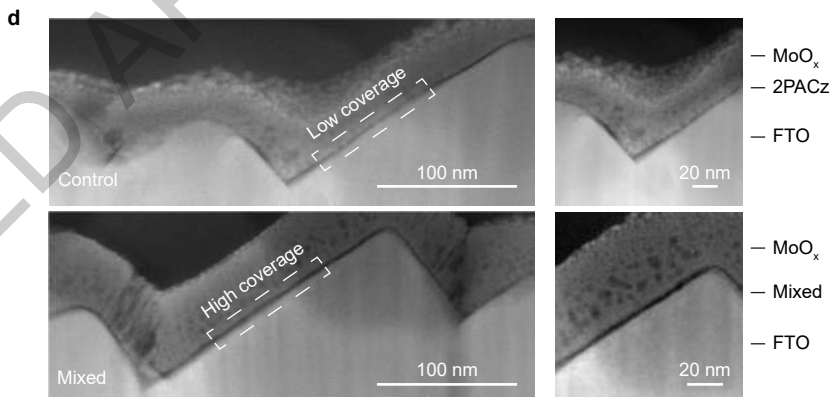
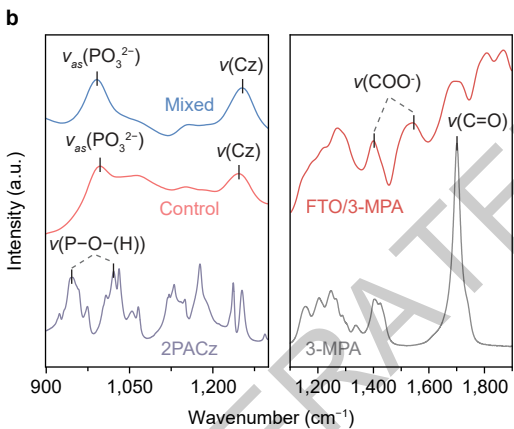
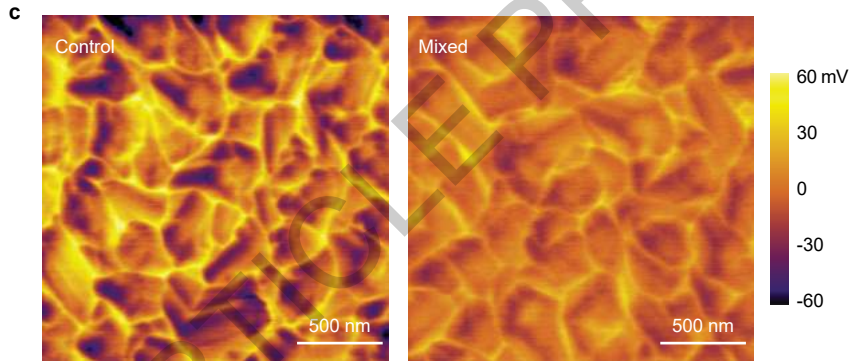
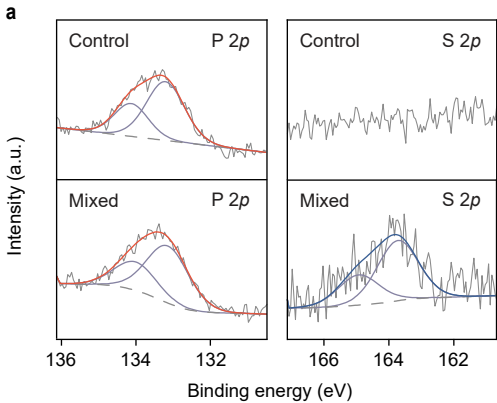
a

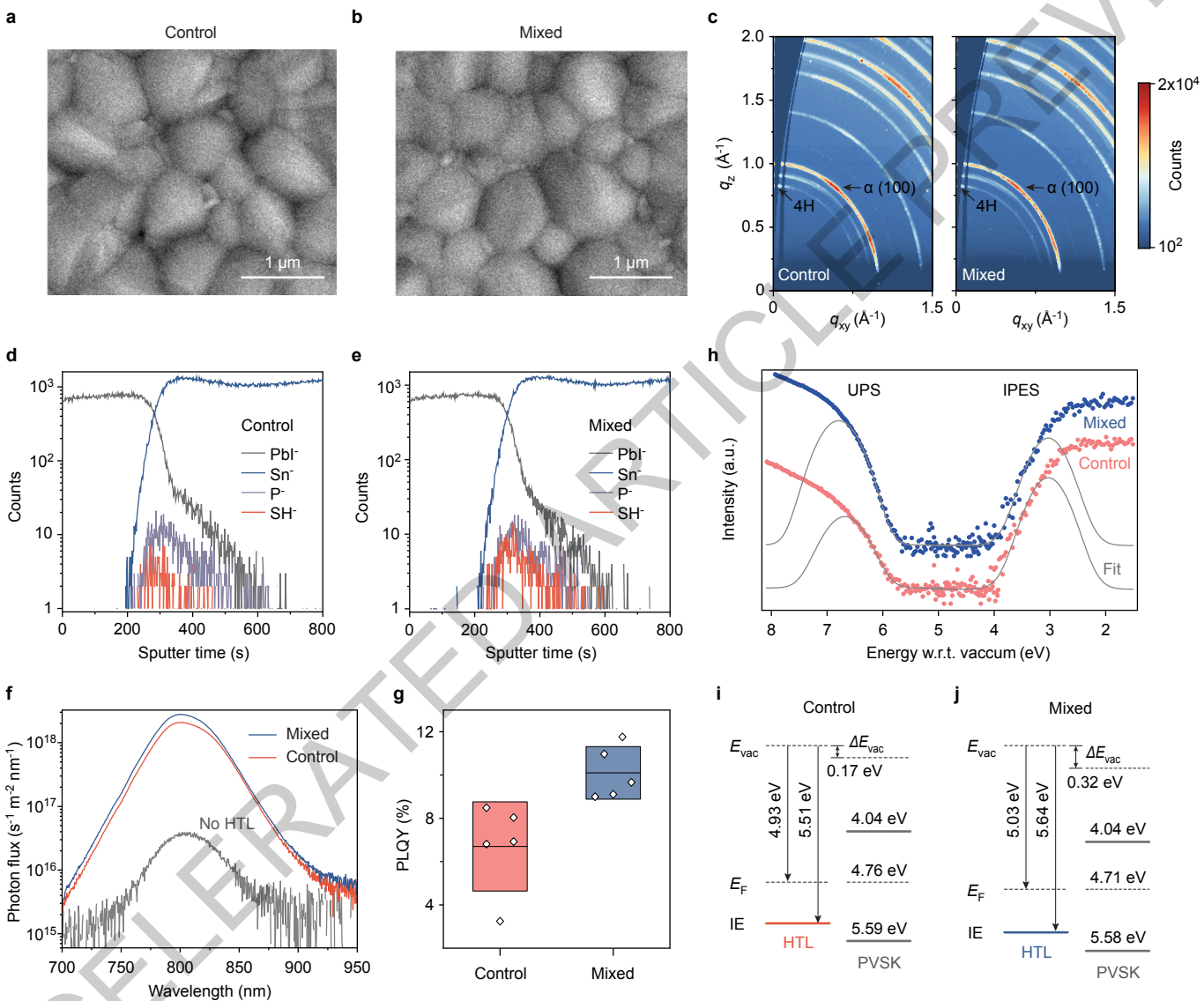
2PACz

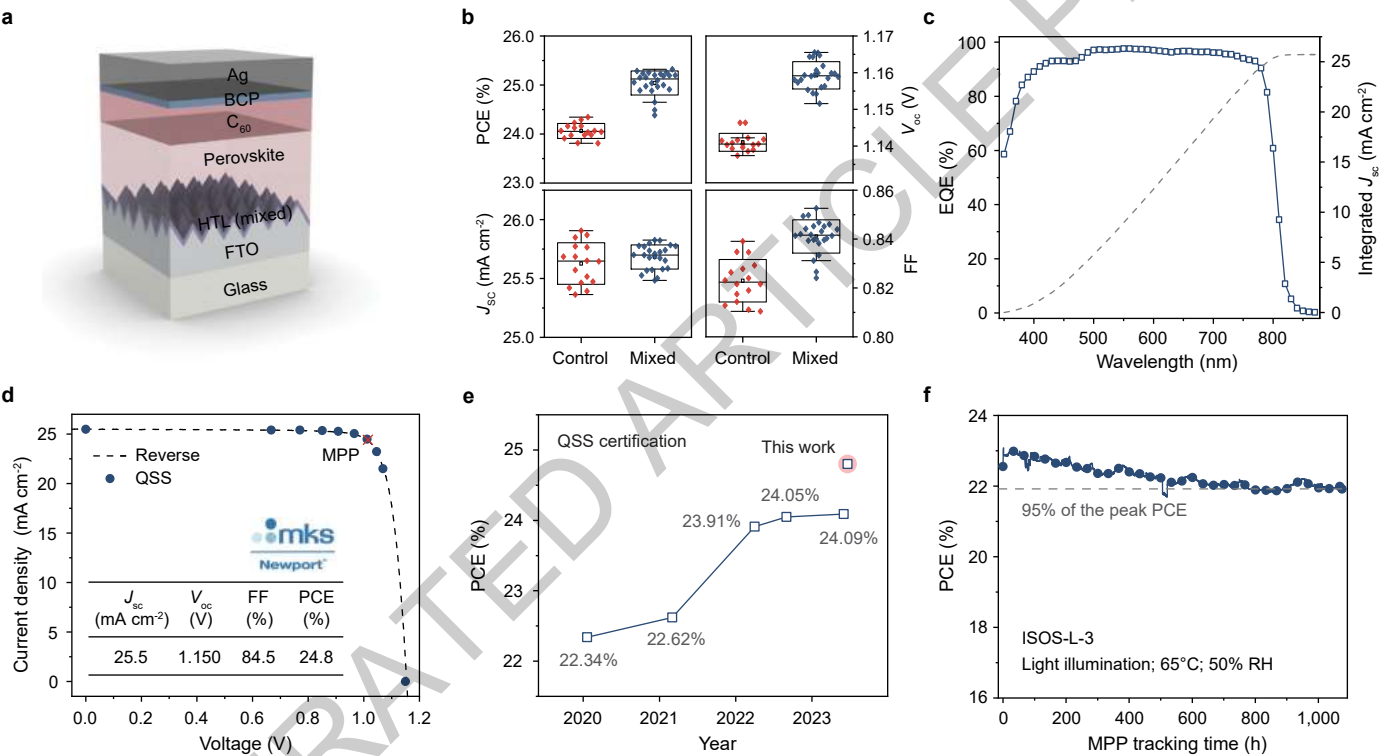


3-MPA

d**e****b****c****f**







Solar Cells Reporting Summary

Nature Research wishes to improve the reproducibility of the work that we publish. This form is intended for publication with all accepted papers reporting the characterization of photovoltaic devices and provides structure for consistency and transparency in reporting. Some list items might not apply to an individual manuscript, but all fields must be completed for clarity.

For further information on Nature Research policies, including our [data availability policy](#), see [Authors & Referees](#).

► Experimental design

Please check: are the following details reported in the manuscript?

1. Dimensions

- Area of the tested solar cells Yes 0.049 cm²
 No
- Method used to determine the device area Yes The active area was determined by the aperture shade mask (0.049 cm²) placed in front of the solar cell
 No

2. Current-voltage characterization

- Current density-voltage (J-V) plots in both forward and backward direction Yes Figure 4d (reverse and quasi-steady-state scans)
 No
- Voltage scan conditions Yes Supplementary Figure 21
For instance: scan direction, speed, dwell times
 No
- Test environment Yes Supplementary Figure 21
For instance: characterization temperature, in air or in glove box
 No
- Protocol for preconditioning of the device before its characterization Yes No preconditioning is needed
 No
- Stability of the J-V characteristic Yes Supplementary Fig. 20b
Verified with time evolution of the maximum power point or with the photocurrent at maximum power point; see ref. 7 for details.
 No

3. Hysteresis or any other unusual behaviour

- Description of the unusual behaviour observed during the characterization Yes PCE from reverse scan matches well with those from the quasi-steady-state scan and steady-state measurements.
 No
- Related experimental data Yes Figure 4d and Supplementary Fig. 20
 No

4. Efficiency

- External quantum efficiency (EQE) or incident photons to current efficiency (IPCE) Yes Figure 4c
 No
- A comparison between the integrated response under the standard reference spectrum and the response measure under the simulator Yes The difference was found to be less than 1.5% (Main text - Solar cell efficiency and stability)
 No
- For tandem solar cells, the bias illumination and bias voltage used for each subcell Yes Not relevant
 No

5. Calibration

- Light source and reference cell or sensor used for the characterization Yes Methods - Solar cell characterization
 No
- Confirmation that the reference cell was calibrated and certified Yes Methods - Solar cell characterization
 No

| | | |
|---|--|--|
| Calculation of spectral mismatch between the reference cell and the devices under test | <input checked="" type="checkbox"/> Yes <input type="checkbox"/> No | M = 1.019 for the certified device |
| 6. Mask/aperture | | |
| Size of the mask/aperture used during testing | <input checked="" type="checkbox"/> Yes <input type="checkbox"/> No | 0.049 cm ² |
| Variation of the measured short-circuit current density with the mask/aperture area | <input type="checkbox"/> Yes <input checked="" type="checkbox"/> No | The accuracy of short-circuit current density was confirmed from EQE measurements. |
| 7. Performance certification | | |
| Identity of the independent certification laboratory that confirmed the photovoltaic performance | <input checked="" type="checkbox"/> Yes <input type="checkbox"/> No | Newport |
| A copy of any certificate(s) <i>Provide in Supplementary Information</i> | <input checked="" type="checkbox"/> Yes <input type="checkbox"/> No | Supplementary Figure 21 |
| 8. Statistics | | |
| Number of solar cells tested | <input checked="" type="checkbox"/> Yes <input type="checkbox"/> No | Figure 4b and Supplementary Figure 22 |
| Statistical analysis of the device performance | <input checked="" type="checkbox"/> Yes <input type="checkbox"/> No | Figure 4b and Supplementary Figure 22 |
| 9. Long-term stability analysis | | |
| Type of analysis, bias conditions and environmental conditions <i>For instance: illumination type, temperature, atmosphere humidity, encapsulation method, preconditioning temperature</i> | <input checked="" type="checkbox"/> Yes <input type="checkbox"/> No | Figure 4f, Supplementary Figure 26 and Supplementary Figure 28 |